Science

RESEARCH ARTI

Check for updates

Cite as: S. Yu *et al.*, *Science*
10.1126/science.adj8858 (2023).

Homogenized NiO_x nanoparticles for improved hole transport in inverted perovskite solar cells

Shiqi Yu[1,2]†, Zhuang Xiong[1,2]†, Haitao Zhou[1,2], Qian Zhang[1,2], Zhenhan Wang[1,2], Fei Ma[1,2], Zihan Qu[1,2], Yang Zhao[1,2], Xinbo Chu[1,2], Xingwang Zhang[1,2], Jingbi You[1,2]*

[1]Key Laboratory of Semiconductor Materials Science, Institute of Semiconductors, Chinese Academy of Sciences, Beijing, P. R. China, 100083. [2]Center of Materials Science and Optoelectronics Engineering, University of Chinese Academy of Sciences, Beijing, P. R. China, 100049.

†These authors contributed equally to this work.

*Corresponding author. Email: jyou@semi.ac.cn

The power conversion efficiency (PCE) of inverted perovskite solar cells (PSCs) is still lagging behind that of conventions PSCs in part because of inefficient carrier transport and poor morphology of hole transport layers (HTLs). We optimized self-assembly of [4-(3,6-dimethyl-9H-carbazol-9-yl)butyl]phosphonic acid (Me-4PACz) onto nickel oxide (NiO_x) nanoparticles as an HTL through treatment with hydrogen peroxide, which created a more uniform dispersion of nanoparticles with high conductivity attributed to formation of Ni^{3+} as well as surface hydroxyl groups for bonding. A 25.2% certified PCE for a mask size of 0.074 cm^2 was obtained. Along this device maintaining 85.4% of the initial PCE after 1000 hours of stabilized power output operation under 1 sun light irradiation at ~ 50 Celsius, and 85.1% of the initial PCE after 500 hours accelerated aging at 85 Celsius. We obtained a PCE of 21.0% for a minimodule with an aperture area of 14.65 cm^2.

Metal halide perovskite solar cells (PSCs) with inverted (p-i-n) structures have certified achieved power conversion efficiencies (PCEs) as high as 24% and have better long-term stability under light and heat stresses compared to the more efficient n-i-p structures (*1*–*4*). Organic materials such as 2,4,6-trimethylphenyl)amine (PTAA) often used as hole-transport layers (HTLs) suffer from low conductivity, hydrophobicity, and energy level mismatch (*5*–*7*).

Recently, self-assembled monolayers (SAMs) such as Me-4PACz, [2-(3,6-dimethoxy-9H-carbazol-9-yl)ethyl]phosphonic acid (MeO-2PACz) series have been successfully used in PSCs [Were these introduced to boost PCE, address the stability issues, or both] (*8*, *9*). However, SAM bonding with transparent conductive oxide substrates such as indium tin oxide (ITO) and fluoride-doped tin oxide (FTO) may not be strong enough to create a homogeneous distribution on the substrate needed to avoid a broad device-performance distribution (*8*, *10*). Several recent results showed that p-type nickel oxide (NiO_x) could form stronger chemical bonding with the SAM layer compared with ITO or FTO, and help to deposit homogeneous SAM (*10*–*12*) and could further deliver better device performance and reproducibility (*13*, *14*).

A high-quality p-type NiO_x HTL needs to be compact to ensure better SAM deposition quality and reduce interface, recombination and also highly conductive. We developed a simple dopant-free method to modulate the NiO_x nanoparticle (NP) solution by adding H_2O_2 solvent. Incorporation of H_2O_2 improved the dispersion of NiO_x NPs and avoided particle aggregation that would inhibit full coverage of the transparent conductive oxide (TCO) substrate. This approach also increased the ratio of Ni^{3+} in NiO_x and formed NiOOH, a stable component that also has high conductivity. The Me-4PACz SAM that formed homogenously on the modulated NiO_x surface was more favorable for the growth of the perovskite and uniform deposition of large-area perovskite by reducing the contact angle, which improved charge extraction and lower leakage currents. As a result, the modulated NiO_x combined with SAM bilayer-based devices exhibited the champion efficiency of 25.5% (Newport certified stabilized efficiency: 25.2%), the 0.1 cm^2 size devices retained 85.4% and 85.1% of the initial efficiency after 1000 hours operation under AM1.5G light illumination at 50°C and 500 hours continuous thermal stress at 85°C, respectively. In addition, a large-area device with 14.65 cm^2 had a PCE of 21%.

HTL layer synthesis and characterization

We observed that H_2O_2 could interact with commercial NiO_x NPs (nominal size 10 nm) and improve the dispersion in aqueous solvent (figs. S1 and S2). High-resolution transmission electron microscopy (HRTEM) showed that the control NiO_x NPs aggregated and the typical size is over 10 nm (Fig. 1A). After H_2O_2 addition, the aggregation was suppressed and the single particle size also decreases to ~5 nm (Fig. 1B). Dynamic light scattering (DLS) confirmed that the statistically average dispersion NP size decreased from 12 to 9 nm after H_2O_2 treatment with much narrow particle-size distribution (Fig. 1C). The formation of hydrated NiO_x through reaction with H_2O_2 likely inhibited NiO_x NP aggregation, enhance

dispersion, and decrease the NP size (*15*).

The effect of the NP size and dispersion distribution on the growth of NiO_x films was reflected in the morphologies of the NiO_x films deposited on FTO substrate. The H_2O_2-modulated NiO_x film was more compact and uniform compared with the control sample. Cross-sectional scanning electron microscopy (SEM) images (fig. S3) revealed the modulated NiO_x film was dense and conformal. Cross-sectional transmission electron microscopy (TEM) and energy dispersive spectroscopy (EDS) mapping results(fig. S4) further confirm this finding. . The root-mean-square (rms) roughness of NiO_x film was reduced from 4.4 nm to 3.2 nm and 2.9 nm after adding 20 mol% H_2O_2 and 40 mol% H_2O_2, respectively (fig. S5). The improvement of the NiO_x morphology was expected to reduce the leakage current and recombination when applied as HTLs in perovskite devices.

X-ray photoelectron spectroscopy (XPS) was performed to investigate the chemical states of the deposited NiO_x thin film. For the NiO_x film, with and without H_2O_2-modulation, the Ni 2p spectrum showed peaks at 857.1, 855.8 and 854.1 eV, which represent the Ni^{4+}, Ni^{3+} and Ni^{2+} species, respectively (Fig. 1, D and E) (*16*). Usually, Ni^{3+} originates from the Ni vacancies and mainly distributes in the grain boundaries of non-stoichiometric oxygen-rich NiO_x (*17, 18*), which is beneficial for hole transport. As illustrated in the Ni 2p spectrum, the ratio of Ni^{3+} increased from 31.3% to 38.3%, was evidence for the generation of Ni vacancies in H_2O_2-modulated sample. In the O 1s spectrum (fig. S6), we assigned peaks at binding energies of 529.5, 531.0, 532.2, and 533.2 eV to the NiO, hydroxide (-OH), Ni^{3+}-O and Ni^{4+}-O, respectively (*16*). The ratio of -OH decreased from 29.6% to 22.4% in H_2O_2-modulated sample. On the contrary, the ratio of Ni^{3+}-O increases from 11.2% to 18.35%, which is likely caused by the transition from $Ni(OH)_2$ to NiOOH in H_2O_2-modulated NiO_x film. The presence of NiOOH could not only improve the conductivity of NiO_x films (*19*), but also provide more surface hydroxyl groups for SAM bonding (*20*).

Both FTIR and Raman spectroscopy further verified the conversion from $Ni(OH)_2$ to NiOOH. The FTIR absorption peaks at 410 cm^{-1} and 500 cm^{-1} in the control NiO_x film, which we assigned to the bending vibration modes of γ(Ni-OH) and δ(Ni-OH), respectively (*21, 22*), were absent in the H_2O_2-modulated NiO_x sample and indicating the reaction $Ni(OH)_2$ inside the treated film (Fig. 1F). In the Raman spectrum (fig. S7), the intensity of 2LO (1075 cm^{-1}) was suppressed in the H_2O_2-modulated NiO_x. The intensity of 2LO is inversely proportional to the concentration of Ni^{3+} inside NiO_x (*23*), so this result was consistent with decreased density of Ni^{3+} in the H_2O_2-modulated samples.

Conductive-mode atomic force microscope (C-AFM) results also indicated that the conductivity of NiO_x has been increased obviously after modulation (fig. S8). For the NiO_x film mobility, it was increased from 2.24×10^{-4} to 2.03×10^{-3} $cm^2V^{-1}s^{-1}$ after treatment based on space-charge-limited current (SCLC) measurement (fig. S9) (*24*). We found that the both the control and modulated NiO_x can keep its original electrical properties after aging at 85°C for 100 hours (fig. S10).

Kevin probe microscopy (KPFM) was used to measure the surface potential distribution of Me-4PACz on the different substrates (FTO, FTO/control NiO_x, and FTO/modulated NiO_x, respectively (Fig. 2, A to C). The line profile comparison of KPFM as depicted in Fig. 2, D to F. Although Me-4PACz could cover most of the FTO substrate, some inhomogeneous regions were present. The SAM layer coverage was more uniform after inserting a NiO_x buffer layer, which could be caused by bonding between PA group and surface hydroxyl groups of the NiO_x, through strong P-O···Ni or P=O···Ni bonds (*20*). As expected, Me-4PACz was almost fully-uniform assembled on the FTO/modulated NiO_x substrates, indicating that condensed and uniform NiO_x layer with more surface hydroxyl groups provided a better site for the growth of high-quality SAM layer.

X-ray photoelectron spectroscopy (XPS) confirmed improved chemical absorption of SAM layer molecular on the NiO_x substrates (Fig. 2, G to I). For the SAMs deposited on the FTO substrate, the P $2p_{1/2}$ and $2p_{3/2}$ core energy level was observed at 133.9 and 133.1 eV, respectively, indicative of Me-4PACz binding (*25*). The presences of an Sn 4s peak at 138.9 eV indicated incomplete coverage of the FTO surface. After inserting the NiO_x layer, the P 2p peak integrated intensity increased by 2.35 times compared with the FTO/SAM sample, indicating a dense and uniform deposition of SAM on NiO_x substrate, The integrated intensity of P 2p increased to 3.0 times on modulated NiO_x substrates compared with deposited on FTO directly. In addition, t the Sn 4s peak has almost disappeared, consistent with full coverage of modulated NiO_x on the FTO substrate.

The energy levels for a very thin film can vary with the thicknesses and also be affected the underlying substrate (*26*). We used ultraviolet photoelectron spectroscopy (UPS) to measure the highest occupied molecular orbital (HOMO) of Me-4PACz deposited on different surfaces, which were -5.35, -5.62, and -5.68 eV for FTO, control NiO_x, and modulated NiO_x surface, respectively (fig. S11). The value of HOMO levels is more consistent with the intrinsic properties of Me-4PCAz (*27*) when depositing on NiO_x surface, which could be the result of better SAM coverage on NiO_x. We also measured the band structure of perovskite nearly pure $FAPbI_3$ we used. The calculated valence band of perovskite at -5.67 eV (fig. S12), was near the HOMO level of the modulated NiO_x/SAM interface (-5.68 eV). These band alignment value could lead to small energy loss at the interface for solar cells devices (fig. S13 and table S1).

We also measured contact angles to study the wetting properties of the different surfaces (Fig. 3, A to C). The perovskite precursor on Me-4PACz-only substrates had a large contact angle of 39.8°, which is consistent with previous reports that perovskite deposition on Me-4PACz surface is relatively challenging (*20*, *28*). The contact angle decreased to 27.4° on control NiO_x/Me-4PACz surface, and further decreased to 20.6° on modulated NiO_x/Me-4PACz surface, indicating that the NiO_x buffer layer enabled better wetting for perovskite growth. Improved hydrophilicity could be due to formation of homogeneous SAM (*9*) or the NiO_x with more hydroxyl groups (fig. S6). The top perovskite layers had similar morphologies (fig. S14). We also examined the morphologies of the buried surface of perovskite layer in contact with the charge transport layer by peeling off the perovskite layer from the substrate (*9*). No obvious morphology defects such as pinholes were observed for the perovskite film deposited on Me-4PACz only surface, which could be caused by the dewetting of the Me-4PACz surface (Fig. 3D). After inserting NiO_x layer between SAM and FTO, the bottom surface of perovskite became denser, and the crystal was more homogeneous (Fig. 3, E and F).

We studied the charge transfer and also the recombination properties at the perovskite buried interface using photoluminescence (PL) and time-resolved photoluminescence (TRPL) measurements with the stack of FTO/HTL/perovskite; for comparison, the results of perovskite directly deposited on FTO were also included (Fig. 3, G and H). The PL intensity of perovskite deposited on SAM surface was greater than that on the FTO surface (Fig. 3G), indicating that the SAM could passivate the buried surface of the perovskite layer (*8*). The PL intensity gradually increased with the coverage of the SAM, inferring that the more compact SAM surface provide more passivation sites for perovskite layer. In addition to the PL enhancement, a blue shift from 815 to 809 nm was observed, further confirming suppression of the interface recombination.

The perovskite TRPL results could be fit by two exponent decays, except for the film on FTO directly (Fig. 3H). The fast decay we attributed to the charge extraction (*29*). The lifetimes were 54, 46, and 42 ns for Me-4PACz, control NiO_x/Me-4PACz, and modulated NiO_x/Me-4PACz, respectively, indicating that the hole extraction became more efficient after inserting and modulating of the NiO_x. This improvement could have resulted from the better coverage of SAM layer (Fig. 2) and also the enhanced electronic properties of the NiO_x (fig. S9). A longer decay time was observed for all perovskites on SAM layers; the perovskite on SAM only had lifetime of 0.7 μs, but was 2.3 μs for the modulated NiO_x surface (Fig. 3H), which indicated that the fully covered Me-4PACz well passivated the buried interface of the perovskite.

Photovoltaic properties

We fabricated the devices with the architecture of glass/FTO/NiO_x/Me-4PACz/$FAPbI_3$/PCBM/SnO_2/Cu, where PCBM is [6,6]-phenyl-C_{61}-butyric acid methyl ester. The fabrication details can be found in Supplementary information. $FAPbI_3$ was used as the perovskite absorber with a bandgap around 1.52 eV, and the thickness of perovskite film was ~ 700 nm with large grains spanning the film. The grain size was ~ 1 μm, as determined from the cross-sectional and top-view SEM images (figs. S14 and S15). The NiO_x layer improved the device performance (Fig. 4A). For the device based on Me-4PACz without NiO_x, the PCE for an illuminated area of 0.1 cm^2 was 22.2% with V_{OC} of 1.11 V, J_{SC} of 26 mA/cm^2, and FF of 77.1%. For devices with the NiO_x layer, the V_{OC} and FF increased to 1.14 V and 81.1%, respectively, and a PCE of 24.1% was achieved. For PSCs based on H_2O_2-modulated NiO_x, a PCE up to 25.6% was achieved with a V_{OC} of 1.16 V, J_{SC} of 26.15 mA/cm^2 and FF of 84.1% (Fig. 4A). We also found that the modulated NiO_x/SAM devices showed neglected hysteresis compared with the NiO_x without modification (Fig. 4B and fig. S16). The detailed device parameters are listed in tables S2 and S3. To show the enhancement after NiO_x insertion is universal, we replaced the substrates and self-assembled molecular by using ITO (indium tin oxide) and MeO-2PACz ((2-(3,6-Dimethoxy-9H-carbazol-9-yl)ethyl)phosphonic acid), respectively, similar trend was observed even though the device performance is not optimized (figs. S17 and S18 and tables S4 and S5).

The typical external quantum efficiency (EQE) result of the device was shown in fig. S19, which is almost consistent with the J_{SC} from current density-voltage (*J-V*) sweeps. We sent one of our best-performing PSC was sent to an accredited laboratory (Newport Corporation PV Lab, USA) for certification. The device with an illuminated mask area of 0.074 cm^2 delivered a certified quasi-steady-state (QSS) efficiency of 25.2% with a V_{OC} of 1.18 V, J_{SC} of 26.2 mA/cm^2, and FF of 81.2% (fig. S20). Compared with the in-house measurement results, we found that the certificated results showed 2% reduction in fill factor, which could be due to the contact degradation during the transportation. Moreover, we collected the PV parameters of 50 devices for each condition (control and H_2O_2-modulated) in fig. S21. The high reproducibility was evidenced by the narrow PCE distribution, and the average PCE with modulation increased from 23.5% to 25.0%, which mainly reflected increases in V_{OC} and FF.

The reverse leakage after introducing NiO_x layer was reduced to more than one order after the modulation of NiO_x by H_2O_2, and also indicated that recombination at the buried surface was suppressed (Fig. 3I). The current density of the NiO_x modulated sample under forward bias was higher than that of SAM only and control NiO_x samples and reflects better charge-transport properties.

We measured transit photovoltage to check and compare charge recombination (fig. S22). The decay time increased from 1.44 μs for SAM only to 2.02 μs for modulated NiO_x/SAM based devices, indicating that the recombination has been suppressed, which was consistent TRPL results (Fig. 3H). We also measured the V_{OC}-light intensity dependent (fig. S23) and found that the ideality factor for the device without NiO_x is 1.71, and indicator of substantial recombination in the SAM only device, With the NiO_x layer, the ideal factor reduced to 1.50, and decreased to 1.22 for modulated NiO_x based devices, which is near the value of 1.14 for the champion normal structure (n-i-p) devices (*30*).

We also studied the electroluminescence performance of the devices working as a light-emitting diodes. The modulated-NiO_x device had a 2.53% external quantum efficiency, versus 0.32% for the Me-4PACz device (fig. S24). This ~8 factor EL enhancement was consistent with a 50 meV V_{OC} increase (Fig. 4A). We conclude that increase in V_{OC} was mainly caused by suppression the defect-related recombination. For the FF and hysteresis improvement, the better physical contact from improved wetting (Fig. 2, A to C) and improved charge transport from better band alignment (fig. S13) or enhanced NiO_x conductivity (fig. S9) also could play a role.

Large-area devices and device stability

We fabricated the minimodules with 6 subcells with an aperture area of 14.65 cm^2. The structural schematic and photomicrograph of the subcell interconnection region are shown in fig. S25, and details of the minimodule fabrication process can be found in the experimental section. The device parameters were a V_{OC} of 6.9 V connected in series, J_{SC} of 3.87 mA/cm^2, and FF of 78.7%, resulting a PCE of 21% (Fig. 4C and table S6) is among the highest efficiency for the large-area PSCs. Based on the geometry design and also the SEM images of pattern (fig. S25), it can be calculated that the geometric fill factor (GFF) is 94.5%, which still has some room for improvement. Comparing the small device, the performance loss for the mini-module is mainly from the short circuit current and fill factor, it can be further improved by depositing more uniform of perovskite layer.

To check the device stabilities, we first compared the stability of NiO_x-based devices without the SAM layer using the small size device (0.1 cm^2). The H_2O_2 modulated strategy had slightly better stability both in stabilized power output (SPO) tracking at 50°C and accelerated aging testing at 85°C (fig. S26), which could be to the contact improvement (*16*). The device with modulated-NiO_x/Me-4PACz bilayer (small size devices: 0.1 cm^2) maintained ~ 79% of its initial PCE of 24.1% at maximum power point (MPP) tracking under 1-sun illumination at 50°C (figs. S27 and S28). The device used for stability did not have an antireflection coating, leading to a 2% less in J_{sc} compared with the champion devices.

We then fabricated a device in which we deposited a 5-nm layer of ITO between Cu electrode and SnO_2 to avoid diffusion. This device retained 85.4% of its initial 23.6% PCE (fig. S29A) after continuous operation for 1000 hours at 50°C (Fig. 4D), tested under MPP tracking the continuous bias voltage of 1.02 V. The enhanced stability of the device after inserting ITO buffer layer could be caused by suppression of ion migration under external stress.

We also investigated the stability of the minimodule. After 400 hours SPO tracking, the device still showed its 90% of its original PCE of 20.5% original efficiency minimodule under 1-sun illumination at 50°C. (figs. S30 and S31). The small-size unencapsulated device with an initial PCE 23.5% without antireflection coating (fig. S29B) was subjected to accelerated aging stability by heated at 85°C in nitrogen condition. The device retained 85.1% of the initial PCE after 500 hours (fig. S32).

Discussion

Self-assembled molecular was widely used for designing efficient inverted perovskite solar cells, the inhomogeneous SAM could lead to the leakage and also the recombination, which limit the device performance and also the reproducibility. We have incorporated homogeneous NiO_x nanoparticles for better SAM growth, based on this hole selecting layer, a small size PSCs with certificate efficiency of 25.2% and 14.6 cm^2 mini-module with 21% efficiency were obtained, and the configured devices own good stability. Further improvement in device performance could be achieved by optimizing the buried and also the top surface. Depositing more uniform perovskite layer will be helpful for further enhancing module devices performance. The bilayer HSL could not only be used in the solar cells, and could be used in other optoelectronic devices such as light-emitting diodes and photodetectors.

REFERENCES AND NOTES

1. Q. Jiang, J. Tong, Y. Xian, R. A. Kerner, S. P. Dunfield, C. Xiao, R. A. Scheidt, D. Kuciauskas, X. Wang, M. P. Hautzinger, R. Tirawat, M. C. Beard, D. P. Fenning, J. J. Berry, B. W. Larson, Y. Yan, K. Zhu, Surface reaction for efficient and stable inverted perovskite solar cells. *Nature* **611**, 278–283 (2022). doi:10.1038/s41586-022-05268-x Medline
2. X. Li, W. Zhang, X. Guo, C. Lu, J. Wei, J. Fang, Constructing heterojunctions by surface sulfidation for efficient inverted perovskite solar cells. *Science* **375**, 434–437 (2022). doi:10.1126/science.abl5676 Medline
3. Z. Li, B. Li, X. Wu, S. A. Sheppard, S. Zhang, D. Gao, N. J. Long, Z. Zhu, Organometallic-functionalized interfaces for highly efficient inverted perovskite solar cells. *Science* **376**, 416–420 (2022). doi:10.1126/science.abm8566 Medline
4. H. Chen, S. Teale, B. Chen, Y. Hou, L. Grater, T. Zhu, K. Bertens, S. M. Park, H. R. Atapattu, Y. Gao, M. Wei, A. K. Johnston, Q. Zhou, K. Xu, D. Yu, C. Han, T. Cui, E. H. Jung, C. Zhou, W. Zhou, A. H. Proppe, S. Hoogland, F. Laquai, T. Filleter, K. R. Graham, Z. Ning, E. H. Sargent, Quantum-size-tuned heterostructures enable efficient and stable inverted perovskite solar cells. *Nat. Photonics* **16**, 352–358 (2022). doi:10.1038/s41566-022-00985-1
5. X. Wu, D. Gao, X. Sun, S. Zhang, Q. Wang, B. Li, Z. Li, M. Qin, X. Jiang, C. Zhang, Z.

Li, X. Lu, N. Li, S. Xiao, X. Zhong, S. Yang, Z. Li, Z. Zhu, Backbone engineering enables highly efficient polymer hole-transporting materials for inverted perovskite solar cells. *Adv. Mater.* **35**, e2208431 (2023). doi:10.1002/adma.202208431 Medline
6. Y. Kim, E. H. Jung, G. Kim, D. Kim, B. J. Kim, J. Seo, Sequentially fluorinated PTAA polymers for enhancing V_{OC} of high-performance perovskite solar cells. *Adv. Energy Mater.* **8**, 1801668 (2018). doi:10.1002/aenm.201801668
7. Z. Ni, C. Bao, Y. Liu, Q. Jiang, W.-Q. Wu, S. Chen, X. Dai, B. Chen, B. Hartweg, Z. Yu, Z. Holman, J. Huang, Resolving spatial and energetic distributions of trap states in metal halide perovskite solar cells. *Science* **367**, 1352–1358 (2020). doi:10.1126/science.aba0893 Medline
8. A. Al-Ashouri, E. Köhnen, B. Li, A. Magomedov, H. Hempel, P. Caprioglio, J. A. Márquez, A. B. Morales Vilches, E. Kasparavicius, J. A. Smith, N. Phung, D. Menzel, M. Grischek, L. Kegelmann, D. Skroblin, C. Gollwitzer, T. Malinauskas, M. Jošt, G. Matič, B. Rech, R. Schlatmann, M. Topič, L. Korte, A. Abate, B. Stannowski, D. Neher, M. Stolterfoht, T. Unold, V. Getautis, S. Albrecht, Monolithic perovskite/silicon tandem solar cell with >29% efficiency by enhanced hole extraction. *Science* **370**, 1300–1309 (2020). doi:10.1126/science.abd4016 Medline
9. S. Zhang, F. Ye, X. Wang, R. Chen, H. Zhang, L. Zhan, X. Jiang, Y. Li, X. Ji, S. Liu, M. Yu, F. Yu, Y. Zhang, R. Wu, Z. Liu, Z. Ning, D. Neher, L. Han, Y. Lin, H. Tian, W. Chen, M. Stolterfoht, L. Zhang, W.-H. Zhu, Y. Wu, Minimizing buried interfacial defects for efficient inverted perovskite solar cells. *Science* **380**, 404–409 (2023). doi:10.1126/science.adg3755 Medline
10. N. Phung, M. Verheijen, A. Todinova, K. Datta, M. Verhage, A. Al-Ashouri, H. Köbler, X. Li, A. Abate, S. Albrecht, M. Creatore, Enhanced Self-Assembled Monolayer Surface Coverage by ALD NiO in p-i-n Perovskite Solar Cells. *ACS Appl. Mater. Interfaces* **14**, 2166–2176 (2022). doi:10.1021/acsami.1c15860 Medline
11. C. Li, X. Wang, E. Bi, F. Jiang, S. M. Park, Y. Li, L. Chen, Z. Wang, L. Zeng, H. Chen, Y. Liu, C. R. Grice, A. Abudulimu, J. Chung, Y. Xian, T. Zhu, H. Lai, B. Chen, R. J. Ellingson, F. Fu, D. S. Ginger, Z. Song, E. H. Sargent, Y. Yan, Rational design of Lewis base molecules for stable and efficient inverted perovskite solar cells. *Science* **379**, 690–694 (2023). doi:10.1126/science.ade3970 Medline
12. J. Sun, C. Shou, J. Sun, X. Wang, Z. Yang, Y. Chen, J. Wu, W. Yang, H. Long, Z. Ying, X. Yang, J. Sheng, B. Yan, J. Ye, NiO_x-Seeded Self-Assembled Monolayers as Highly Hole-Selective Passivating Contacts for Efficient Inverted Perovskite Solar Cells. *Sol. RRL* **5**, 2100663 (2021). doi:10.1002/solr.202100663
13. L. Li, Y. Wang, X. Wang, R. Lin, X. Luo, Z. Liu, K. Zhou, S. Xiong, Q. Bao, G. Chen, Y. Tian, Y. Deng, K. Xiao, J. Wu, M. I. Saidaminov, H. Lin, C.-Q. Ma, Z. Zhao, Y. Wu, L. Zhang, H. Tan, Flexible all-perovskite tandem solar cells approaching 25% efficiency with molecule-bridged hole-selective contact. *Nat. Energy* **7**, 708–717 (2022). doi:10.1038/s41560-022-01045-2
14. C. C. Boyd, R. C. Shallcross, T. Moot, R. Kerner, L. Bertoluzzi, A. Onno, S. Kavadiya, C. Chosy, E. J. Wolf, J. Werner, J. A. Raiford, C. de Paula, A. F. Palmstrom, Z. J. Yu, J. J. Berry, S. F. Bent, Z. C. Holman, J. M. Luther, E. L. Ratcliff, N. R. Armstrong, M. D. McGehee, Overcoming redox reactions at perovskite-nickel oxide interfaces to boost voltages in perovskite solar cells. *Joule* **4**, 1759–1775 (2020). doi:10.1016/j.joule.2020.06.004
15. N. Sasirekha, B. Rajesh, Y.-W. Chen, Synthesis of TiO_2 sol in a neutral solution using $TiCl_4$ as a precursor and H_2O_2 as an oxidizing agent. *Thin Solid Films* **518**, 43–48 (2009). doi:10.1016/j.tsf.2009.06.015
16. M. Du, S. Zhao, L. Duan, Y. Cao, H. Wang, Y. Sun, L. Wang, X. Zhu, J. Feng, L. Liu, X. Jiang, Q. Dong, Y. Shi, K. Wang, S. Liu, Surface redox engineering of vacuum-deposited NiO_x for top-performance perovskite solar cells and modules. *Joule* **6**, 1931–1943 (2022). doi:10.1016/j.joule.2022.06.026
17. Q. Liu, Q. Chen, Q. Zhang, Y. Xiao, X. Zhong, G. Dong, M.-P. Delplancke-Ogletree, H. Terryn, K. Baert, F. Reniers, X. Diao, In situ electrochromic efficiency of a nickel oxide thin film: Origin of electrochemical process and electrochromic degradation. *J. Mater. Chem. C Mater. Opt. Electron. Devices* **6**, 646–653 (2018). doi:10.1039/C7TC04696K
18. J.-L. Yang, Y.-S. Lai, J. S. Chen, Effect of heat treatment on the properties of non-stoichiometric p-type nickel oxide films deposited by reactive sputtering. *Thin Solid Films* **488**, 242–246 (2005). doi:10.1016/j.tsf.2005.04.061
19. X. Cui, J. Jin, J. Zou, Q. Tang, Y. Ai, X. Zhang, Z. Wang, Y. Zhou, Z. Zhu, G. Tang, Q. Cao, S. Liu, X. Liu, Q. Tai, NiO_x nanocrystals with tunable size and energy levels for efficient and UV stable perovskite solar cells. *Adv. Funct. Mater.* **32**, 2203049 (2022). doi:10.1002/adfm.202203049
20. L. Mao, T. Yang, H. Zhang, J. Shi, Y. Hu, P. Zeng, F. Li, J. Gong, X. Fang, Y. Sun, X. Liu, J. Du, A. Han, L. Zhang, W. Liu, F. Meng, X. Cui, Z. Liu, M. Liu, Fully textured, production-line compatible monolithic perovskite/silicon tandem solar cells approaching 29% efficiency. *Adv. Mater.* **34**, e2206193 (2022). doi:10.1002/adma.202206193 Medline
21. M. Casas-Cabanas, M. D. Radin, J. Kim, C. P. Grey, A. Van der Ven, M. R. Palacín, The nickel battery positive electrode revisited: Stability and structure of the β-NiOOH phase. *J. Mater. Chem. A Mater. Energy Sustain.* **6**, 19256–19265 (2018). doi:10.1039/C8TA07460G
22. Y. Ren, W. K. Chim, L. Guo, H. Tanoto, J. Pan, S. Y. Chiam, The coloration and degradation mechanisms of electrochromic nickel oxide. *Sol. Energy Mater. Sol. Cells* **116**, 83–88 (2013). doi:10.1016/j.solmat.2013.03.042
23. A. C. Gandhi, J. Pant, S. D. Pandit, S. K. Dalimbkar, T.-S. Chan, C.-L. Cheng, Y.-R. Ma, Y. W. Sheng, Short-range magnon excitation in NiO nanoparticles. *J. Phys. Chem. C Nanomater. Interfaces* **117**, 18666–18674 (2013). doi:10.1021/jp4029479
24. A. Wang, Z. Cao, J. Wang, S. Wang, C. Li, N. Li, L. Xie, Y. Xiang, T. Li, X. Niu, L. Ding, F. Hao, Vacancy defect modulation in hot-casted NiO_x film for efficient inverted planar perovskite solar cells. *J. Energy Chem.* **48**, 426–434 (2020). doi:10.1016/j.jechem.2020.02.034
25. H. Bin, K. Datta, J. Wang, T. P. A. van der Pol, J. Li, M. M. Wienk, R. A. J. Janssen, Finetuning hole-extracting monolayers for efficient organic solar cells. *ACS Appl. Mater. Interfaces* **14**, 16497–16504 (2022). doi:10.1021/acsami.2c01900 Medline
26. P. Schulz, E. Edri, S. Kirmayer, G. Hodes, D. Cahen, A. Kahn, Interface energetics in organo-metal halide perovskite-based photovoltaic cells. *Energy Environ. Sci.* **7**, 1377–1381 (2014). doi:10.1039/c4ee00168k
27. X. Zheng, Z. Li, Y. Zhang, M. Chen, T. Liu, C. Xiao, D. Gao, J. B. Patel, D. Kuciauskas, A. Magomedov, R. A. Scheidt, X. Wang, S. P. Harvey, Z. Dai, C. Zhang, D. Morales, H. Pruett, B. M. Wieliczka, A. R. Kirmani, N. P. Padture, K. R. Graham, Y. Yan, M. K. Nazeeruddin, M. D. McGehee, Z. Zhu, J. M. Luther, Co-deposition of hole-selective contact and absorber for improving the processability of perovskite solar cells. *Nat. Energy* **8**, 462–472 (2023). doi:10.1038/s41560-023-01227-6
28. Z. Ying, Z. Yang, J. Zheng, H. Wei, L. Chen, C. Xiao, J. Sun, C. Shou, G. Qin, J. Sheng, Y. Zeng, B. Yan, X. Yang, J. Ye, Monolithic perovskite/black-silicon tandems based on tunnel oxide passivated contacts. *Joule* **6**, 2644–2661 (2022). doi:10.1016/j.joule.2022.09.006
29. R. Lin, Y. Wang, Q. Lu, B. Tang, J. Li, H. Gao, Y. Gao, H. Li, C. Ding, J. Wen, P. Wu, C. Liu, S. Zhao, K. Xiao, Z. Liu, C. Ma, Y. Deng, L. Li, F. Fan, H. Tan, All-perovskite tandem solar cells with 3D/3D bilayer perovskite heterojunction. *Nature* **620**, 994–1000 (2023). doi:10.1038/s41586-023-06278-z Medline
30. Y. Zhao, F. Ma, Z. Qu, S. Yu, T. Shen, H. X. Deng, X. Chu, X. Peng, Y. Yuan, X. Zhang, J. You, Inactive $(PbI_2)_2RbCl$ stabilizes perovskite films for efficient solar cells. *Science* **377**, 531–534 (2022). doi:10.1126/science.abp8873 Medline
31. K. Xiao, R. Lin, Q. Han, Y. Hou, Z. Qin, H. T. Nguyen, J. Wen, M. Wei, V. Yeddu, M. I. Saidaminov, Y. Gao, X. Luo, Y. Wang, H. Gao, C. Zhang, J. Xu, J. Zhu, E. H. Sargent, H. Tan, All-perovskite tandem solar cells with 24.2% certified efficiency and area over 1 cm^2 using surface-anchoring zwitterionic antioxidant. *Nat. Energy* **5**, 870–880 (2020). doi:10.1038/s41560-020-00705-5
32. Z. Chu, Y. Zhao, F. Ma, C.-X. Zhang, H. Deng, F. Gao, Q. Ye, J. Meng, Z. Yin, X. Zhang, J. You, Large cation ethylammonium incorporated perovskite for efficient and spectra stable blue light-emitting diodes. *Nat. Commun.* **11**, 4165 (2020). doi:10.1038/s41467-020-17943-6 Medline
33. A. Al-Ashouri, A. Magomedov, M. Roß, M. Jošt, M. Talaikis, G. Chistiakova, T. Bertram, J. A. Márquez, E. Köhnen, E. Kasparavičius, S. Levcenco, L. Gil-Escrig, C. J. Hages, R. Schlatmann, B. Rech, T. Malinauskas, T. Unold, C. A. Kaufmann, L. Korte, G. Niaura, V. Getautis, S. Albrecht, Conformal monolayer contacts with lossless interfaces for perovskite single junction and monolithic tandem solar cells. *Energy Environ. Sci.* **12**, 3356–3369 (2019). doi:10.1039/C9EE02268F

ACKNOWLEDGMENTS

This work was supported by National Key Research and Development Program of China (Grant Number. 2020YFB1506400), National Science Fund for Distinguished Young Scholars (Grant Numbers: 61925405) and CAS Project for

Young Scientists in Basic Research (YSBR-090). We would like to thank Prof. Qi Jiang from Institute of Semiconductors, CAS for discussion, and Prof. Chenyi Yi from Tsinghua University for helping in TPV measurement. **Author contributions:** J. Y., Z. X., and S. Y. conceived the idea. J. Y. directed and supervised the project. S. Y. initialized inverted perovskite solar cells based on NiO_x nanoparticles and developed the device structure. Z. X. modulated NiO_x particles and applied into the inverted perovskite solar cells. Q. Z., H. Z., F. M., Z. Q., Y. Z., X. C., X. Z. were involved in data analysis. Y. Y. was responsible for GIWAXS measurements and analysis. J. Y., S. Y. and. Z. X. cowrote the manuscript, all authors contributed to discussions and finalizing the manuscript. **Competing interests:** A Chinese patent application (CN 202310148064.5) was submitted by the Institute of Semiconductors, Chinese Academy of Sciences, that covers the homogenized NiO_x nanoparticles for efficient inverted perovskite solar cells. **Data and materials availability:** All data needed to evaluate the conclusions in the paper are present in the paper or the supplementary materials.

SUPPLEMENTARY MATERIALS

science.org/doi/10.1126/science.adj8858
Materials and Methods
Figs. S1 to S32
Tables S1 to S6
References (*31*–*33*)

Submitted 13 August 2023; resubmitted 14 September 2023
Accepted 13 November 2023
Published online 23 November 2023
10.1126/science.adj8858

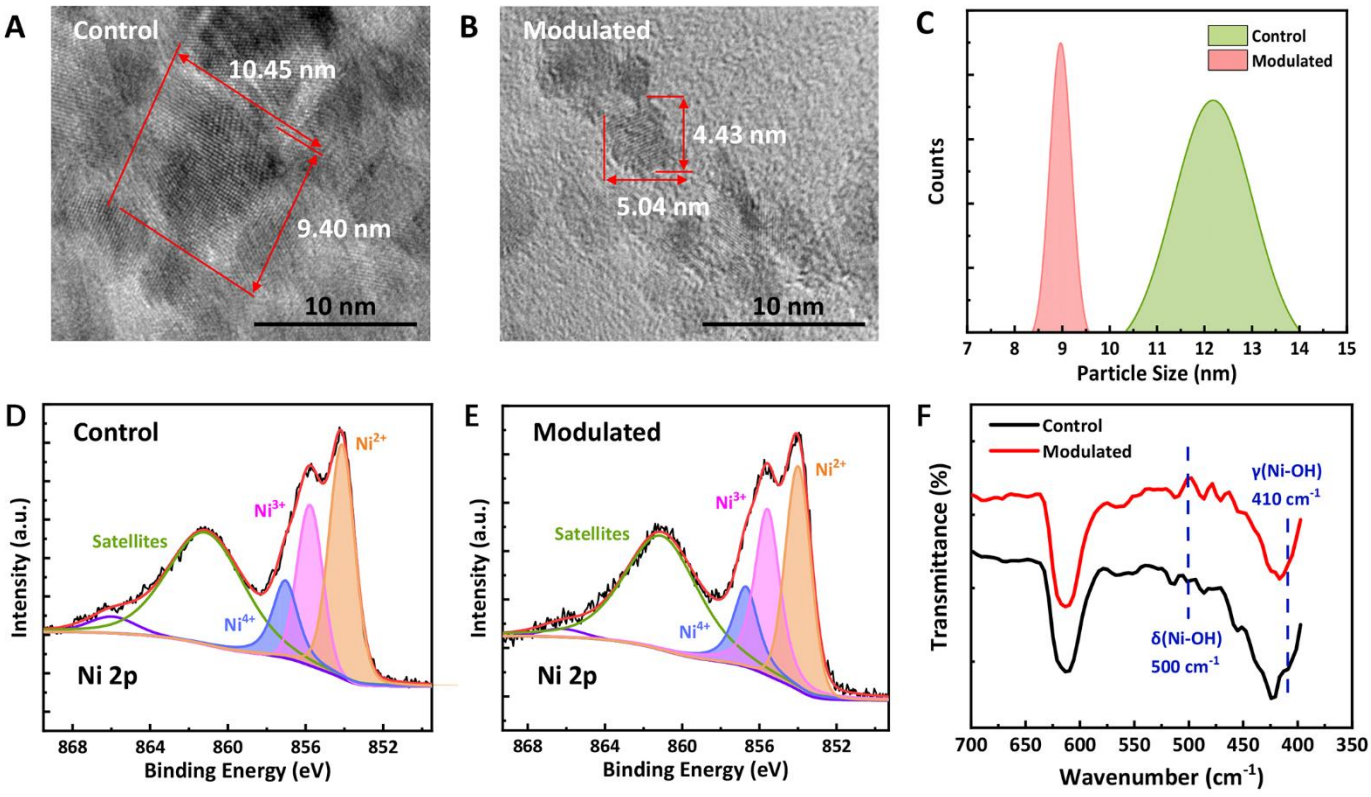

Fig. 1. Characterization of the NiO_x nanoparticles. (A and B) HRTEM images of the control and modulated NiO_x nanoparticles, respectively. (C) Size distribution of control and modulated NiO_x nanoparticles in solvent, which was measured by DLS. (D and E) XPS spectra of Ni 2p core levels for control and H_2O_2-modulated NiO_x films, respectively. (F) FTIR spectra of control and modulated NiO_x nanoparticles in the 400 to 700 cm^{-1} wavenumber region.

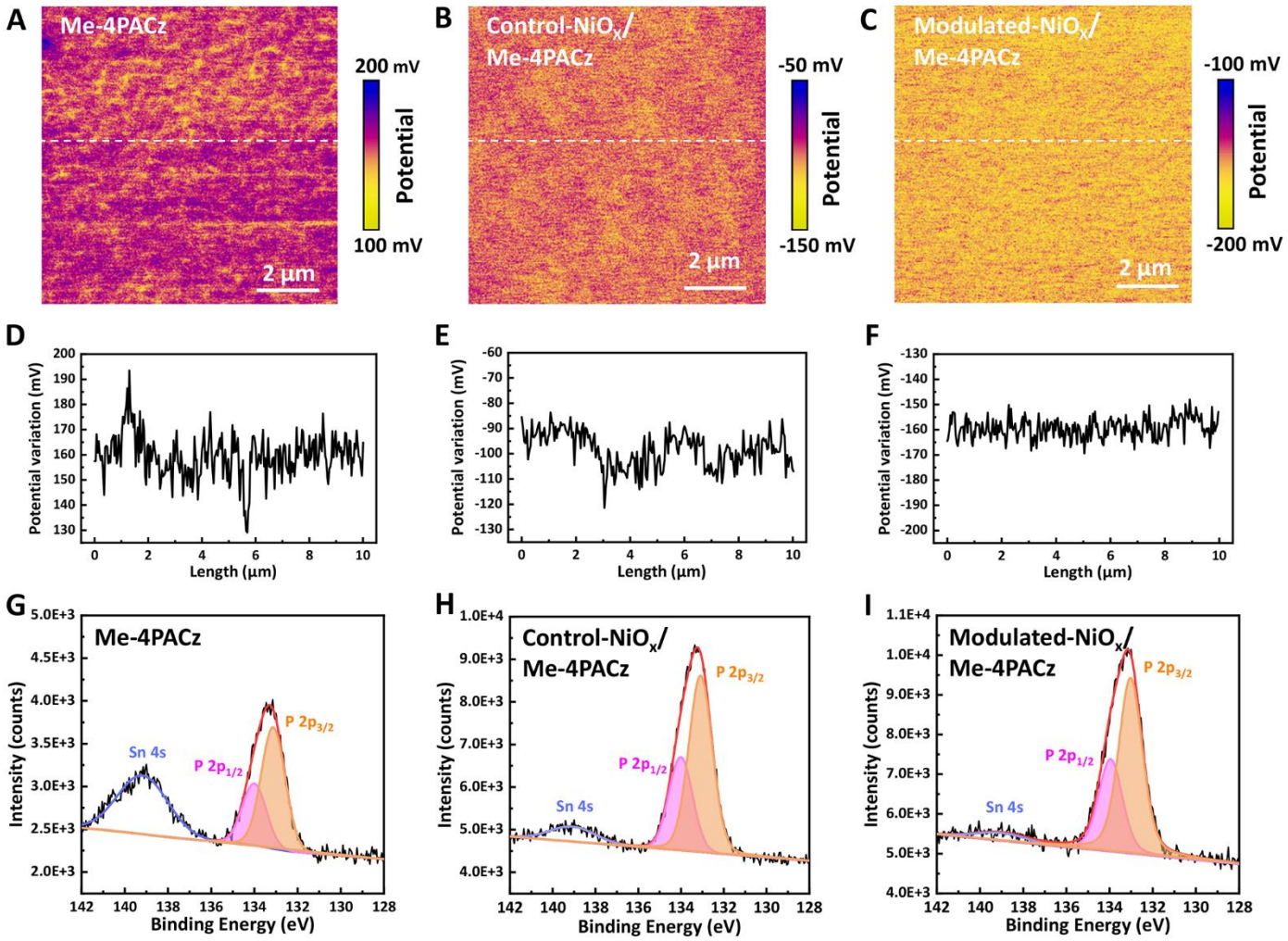

Fig. 2. Characterization of the SAM and NiO_x/SAM layers. (**A** to **C**) KPFM images of surface potential of Me-4PACz, control-NiO_x/Me-4PACz and modulated-NiO_x/Me-4PACz, respectively. (**D** to **F**) Corresponding line profiles of Me-4PACz, control-NiO_x/Me-4PACz and modulated-NiO_x/Me-4PACz, respectively. (**G** to **I**) XPS spectra of P 2p core levels for Me-4PACz, control-NiO_x/Me-4PACz and modulated-NiO_x/Me-4PACz films, respectively.

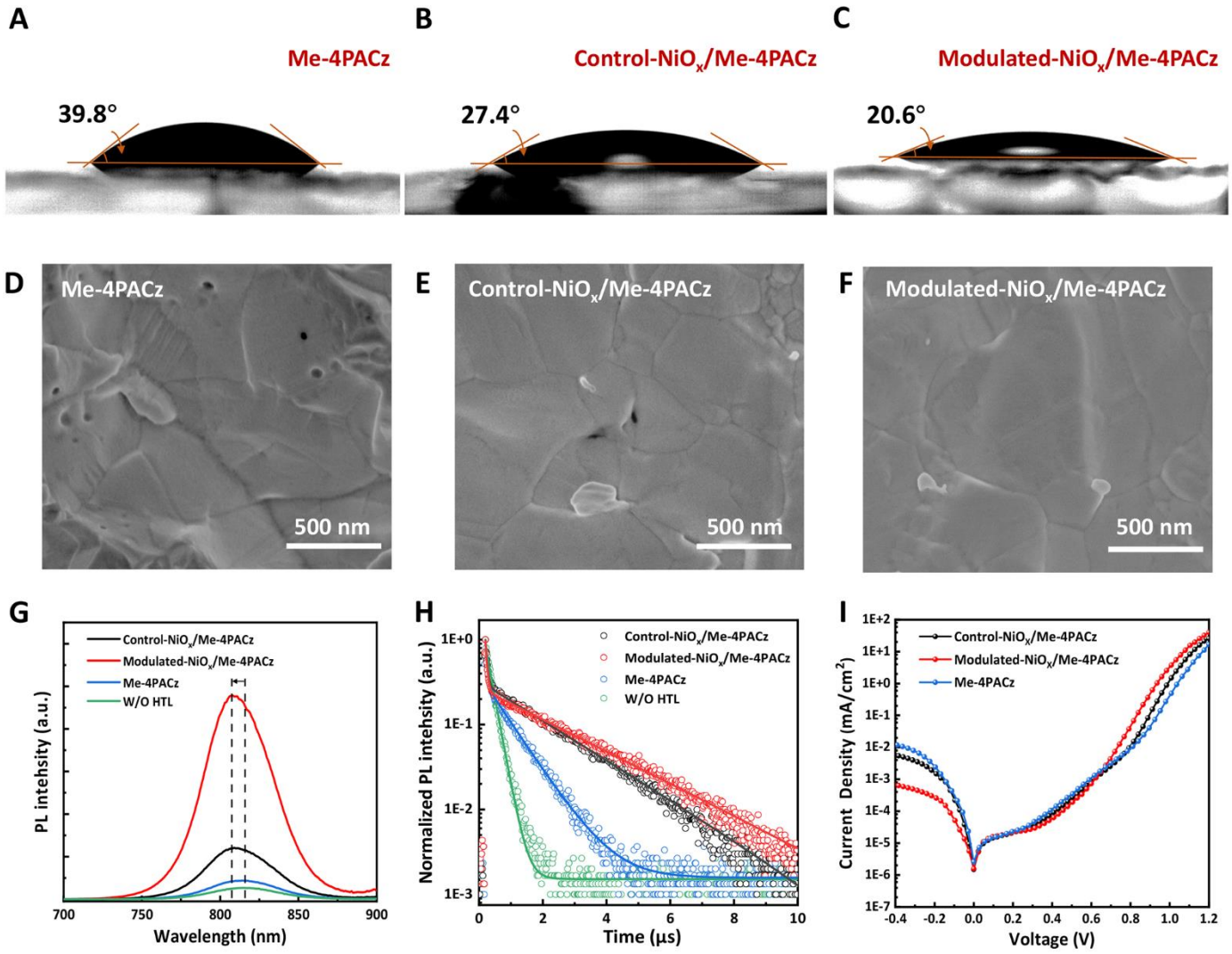

Fig. 3. Surface and electronic properties of SAM and NiO_x/SAM layers. (A to C) Contact angles of the perovskite precursor solution on different HTL layers. (D to F), Top-view SEM images of the bottom surface of perovskite deposited on different HTLs. (G and H) PL and TRPL measurements of perovskite films on different HTL layers. (I) Dark *J-V* measurements of different HTL layers based inverted devices.

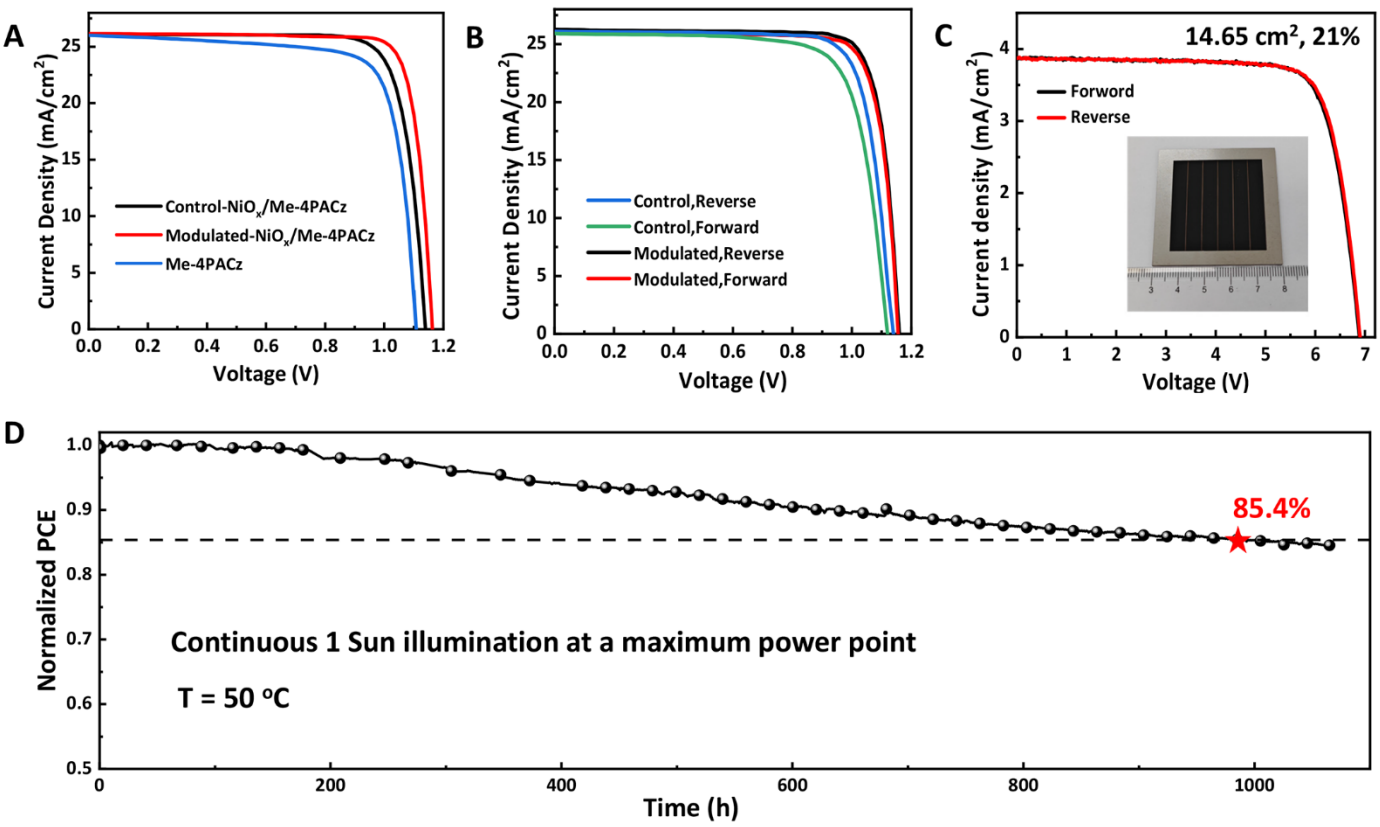

Fig. 4. Photovoltaic performance and stability of devices. (A) *J-V* curves of the Me-4PACz, control-NiO_x/Me-4PACz and modulated-NiO_x/Me-4PACz based devices (device area is 0.108 cm^2, and the mask size is 0.0737 cm^2) measured under AM 1.5G (100 mW/cm^2) illumination. (B) *J-V* curves of the devices under reverse and forward scan for the control-NiO_x and modulated-NiO_x devices, respectively. (C) *J-V* curves of the modulated-NiO_x/Me-4PACz based devices (14.65 cm^2) measured under AM 1.5G (100 mW/cm^2) illumination. (D) Steady power output tracking for the modulated devices (0.1 cm^2), the device was applied bias at maximum power point, under 1-sun illumination at ~50°C, for enhancing the stability, a 5 nm thin film of ITO was used as buffer layer between SnO_2 and Cu.

Homogenized NiO_x nanoparticles for improved hole transport in inverted perovskite solar cells

Shiqi Yu, Zhuang Xiong, Haitao Zhou, Qian Zhang, Zhenhan Wang, Fei Ma, Zihan Qu, Yang Zhao, Xinbo Chu, Xingwang Zhang, and Jingbi You

*Science***Ahead of Print** DOI: 10.1126/science.adj8858

Science (ISSN 1095-9203) is published by the American Association for the Advancement of Science. 1200 New York Avenue NW, Washington, DC 20005. The title *Science* is a registered trademark of AAAS.